Available online at www.sciencedirect.com

jmr&t Journal of Materials Research and Technology

www.jmrt.com.br

Original Article

Photocatalytic activity of electric-arc furnace flue dusts

Lorena Alcaraz[a], Ana Urbieta[b], María Eugenia Rabanal[c], Paloma Fernández[b], Félix A. López[a,*]

[a] Centro Nacional de Investigaciones Metalúrgicas (CENIM-CSIC). Avda. Gregorio del Amo 8. 28040 Madrid, Spain
[b] Universidad Complutense de Madrid (UCM). Dpto. de Física de Materiales. Facultad de Ciencias Físicas. Ciudad Universitaria s/n 28040 Madrid, Spain
[c] Universidad Carlos III de Madrid & IAAB, Dpto. de Ciencia e Ingeniería de Materiales e Ingenieria Química, Avda. de la Universidad 30, 28911-Leganés, Madrid, Spain

ARTICLE INFO

Article history:
Received 3 May 2019
Accepted 19 November 2019
Available online 15 December 2019

Keywords:
EAFD
Photocatalytic activity
Electric steel making waste

ABSTRACT

Two electric-arc furnace flue dusts, a waste generated during the steel production process, were characterized and their photocatalytic activity was assessed. Chemical composition by X-ray fluorescence (XRF) analysis identified that both dusts were principally formed by iron, zinc and chromium oxides. Structural characterization carried out by X-ray diffraction patterns (XRD), and micro-Raman measurements demonstrated that $ZnFe_2O_4$ (zinc ferrite), $FeCr_2O_4$ (chromite) and ZnO (zincite) are present in both waste dusts as majority phases. Scanning electron microscopy (SEM) images showed that both dusts are formed by nanoparticles with a globular and octahedral morphology characteristic of the type of flue dusts formation and the obtained phases. Cathodoluminescence (CL) spectra show the characteristics bands of spinel structure ($ZnFe_2O_4$) and Fe^{3+} emission. X-ray photoelectron spectroscopy (XPS) measurements indicate that Fe ions could be present in 2+ and 3+ oxidation state in the spinel structure, while zinc and chromium ions are in 2+ and 3+, respectively. In addition, the photocatalytic experiments demonstrated that the analyzed samples could be useful as photocatalyzed showing a degradation percentage above 75 %.

1. Introduction

Electric-arc steelmaking flue dusts are a type of solid waste that is produced in the purification of gases given off in furnaces used in steelmaking from smelting scrap metal [1,2]. The EC legislation classifies electric arc furnace dusts (EAFD) a hazardous waste. The EAFD is composed of different components being the principal solid iron oxides as well as zinc. Iron is found as magnetite (Fe_3O_4) and in franklinite ($ZnFe_2O_4$), and zinc is forming zincite (ZnO) and franklinite [3]. Due to the significant amount generated (2–14 kg of dusts per ton of steel; 3.7 million tonnes of EAFD per year) [2], is required different steel recycling alternatives are required [4]. There are different options for treating the obtained EAFD as waste among them (a) the return to the steel production process [5–7], (b) disposal in industrial waste landfills [8] and/or (c) the recycling/incorporation into other processes/products [2,9]. The

* Corresponding author.
E-mail: f.lopez@csic.es (F.A. López).
https://doi.org/10.1016/j.jmrt.2019.11.053

latter is increasingly attracting the interest of the scientific community. Therefore, the possibility of reusing the compounds of which the EAFD is formed for other processes is a way forward.

ZnO has been used as a photocatalytic material due to its high activity as well as chemical stability [10]. However, it has a wide band gap of 3.2 eV, which is unfavorable for absorption and utilization of visible light. Different investigations have been carried out using materials with lower Egap proving the effectiveness for the degradation of organic contaminants in water under solar irradiation [11–13]. In this sense, some spinel materials with narrow band gap such as $ZnFe_2O_4$ (about 1.9 eV) exhibit good visible light response and photochemical stability as well as favorable magnetism [14,15]. The narrow band gap enables it to absorb sunlight up to 653 nm or even larger [16]. However, this material is seldom used as photocatalysts as a single phase due to the lower valence band potential and its poor property in photoelectric conversion yield. For these reasons, the scientific community has been paid more attention to the enhanced photocatalytic activity of $ZnFe_2O_4$/ZnO composite [17,18]. In addition, because of the magnetic behaviour of the $ZnFe_2O_4$ phase, it is possible to easily recover the solid photocatalyst after the photocatalytic process [17].

In this sense, advance oxidation processes (AOP's) have been useful as a novel and variety of green process for different pollutants present in wastewater [19–21]. In general, AOP's are able to generate hydroxyl radicals (OH·) in oxidation processes and degradate aqueous contaminants into innocuous products [20]. In this sense, organic synthetic dyes are commonly utilizing by textile industries. Due to its high stability, the exposure to these contaminants leads to harmful effect on humans and animals. In fact, methylene blue (MB) is a basic cationic dye commonly used for dying wool, cotton, silk, etc, which can cause serious diseases like hard breathing, vomiting, and mental disorders [21].

So, the use of the electric-arc furnace flue dust, a commonly generated waste, as photocatalytic material is a promising alternative to re-use and re-cycling this type of the solid wastes. In the present work, the structural and morphological characterization of two different electric-arc furnace flue dusts, an EAFD from common steel manufacturing (named as C-EAFD) and an EAFD from the manufacturing of special steel (named as S-EAFD) were carried out. In addition, the photocatalytic activity of both samples was also investigated.

2. Materials and methods

In order to investigate the physico-chemical properties of EAFD, two samples were taken at the outlet of the suppression system from Siderurgia Sevillana (Alcalá de Guadaira, Sevilla, Spain) and Fundiciones de Aceros Especiales (Santander, Spain).

The samples were homogenized, and successive quartering provided 1000 g of each sample.

The chemical composition of the samples was determined by X-ray fluorescence (XRF) using the above-mentioned PANalytical Axios wavelength dispersive spectrometer.

The structural characterization was carried out through X-ray diffraction (XRD) using a Siemens D5000 diffractometer equipped with a Cu anode (Cu Kα radiation) and a LiF monochromator. Rietveld method was applied for the calculation of structural parameters from XRD patterns. We have used the version 4.2 of the Rietveld analysis program TOPAS (Bruker ASX) and crystallographic information of the different phases obtained from Pearson's crystal structure database for inorganic compounds release.

The morphological characterization was performed by scanning electron microscopy (SEM) using a JEOL-6400 electron microscope operating at 20 kV.

Micro-Raman measurements were carried out at room temperature (RT) in a Horiba Jovin-Ybon LabRAM HR800 system. The samples were excited by a 632.8 nm He-Ne laser on an Olympus BX 41 confocal microscope with a 40x objective. A charge coupled device detector was used to collect the scattered light dispersed by a 1200 lines mm^{-1} grating.

The surface of both EAFD samples was analyzed by X-ray photoelectron spectroscopy (XPS). Spectra were recorded using a Fisons MT500 spectrometer equipped with a hemispherical electron analyzer (CLAM2) and a non-monochromatic Mg K_α X-ray source operated at 300 W. Spectra were collected at a pass energy of 20 eV (typical for high-resolution conditions). The area under each peak was calculated after subtraction of the S-shaped background and fitting the experimental curve to a combination of Lorentzian and Gaussian lines of variable proportions. Binding energies were calibrated to the C 1s peak at 285.0 eV. The atomic ratios were computed from the peak intensity ratios and reported atomic sensitivity factors.

The temperature dependence of the magnetic susceptibility was measured in the 2–300 K range in a magnetic field of 1000 Oe using a Quantum Design XL-SQUID magnetometer. Hysteresis measurements were taken at 298 K with a maximum field of 5T.

Cathodoluminescence investigations have been performed at room temperature in a HITACHI S2500 SEM operated at 15 kV. Spectra have been recorded with a CCD camera HAMAMATSU PMA-11.

The samples were characterized by UV-visible diffuse reflectance spectra (DRS) measured in the range of 350−500 nm at RT using a UV-visible Spectrophotometer (Varian Cary 100 with DRA-CA-30I Diffuse Reflectance Accessory).

The photocatalysis experiments were carried out in a Pyrex glass reactor at RT. 5 mg of solid catalyst was dispersed in 600 mL of a solution of methylene blue (MB) of concentration 2.5 mg/L. The photocatalytic degradation was carried out for 120 min, in continuous stirring under UV-light irradiation (365 nm), in a dark room with 125 W high-pressure mercury vapor lamp (Jinfei Company, Shanghai). Aliquots (3 mL) of the solution are extracted every 10 min (every 15 min for times larger than 75 min) are measured by UV-Vis absorption in a Lambda 14 P UV-visible Spectrophotometer to monitor the degradation of methylene blue (MB) solution.

Table 1 – Elemental composition (wt %) for both samples obtained.

Compound	C-EAFD	S-EAFD
Fe_2O_3	37.68	38.02
ZnO	30.35	20.14
CaO	8.42	4.44
PbO	5.66	0.67
CdO	3.82	2.80
Cl	3.10	0.93
SiO_2	2.30	7.13
MnO	1.92	2.87
SO_3	1.85	0.48
K_2O	1.81	0.66
MgO	0.97	2.36
Cr_2O_3	0.58	16.97
Al_2O_3	0.57	0.50
CuO	0.45	0.18
SnO_2	0.10	—
TiO_2	0.08	0.19
Br	0.08	0.01
NiO	0.06	1.30
Co_3O_4	0.06	0.08
BaO	0.05	—
V_2O_5	0.03	0.09
Ta_2O_5	—	0.04
Bi_2O_3	—	0.03
Ga_2O_3	—	0.02
MoO_3	0.01	0.11
SrO	0.01	—
Nb_2O_5	—	0.01
ZrO_2	—	0.01

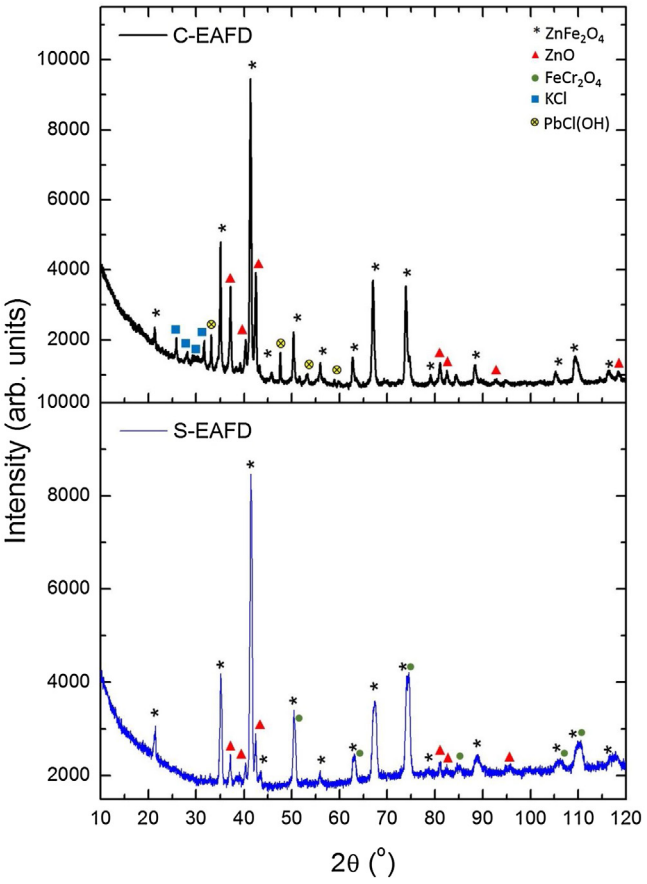

Fig. 1 – XRD patterns of both EAFD dusts.

3. Results and discussion

3.1. *Physico-chemical characterization of EAFD flue dusts*

Table 1 shows the elemental composition of the EAFD samples determined by XRF. Although the composition of EAFD can significantly vary depending on the furnace operating conditions and the scrap quality [4,22,23], the elements that are usually present mostly are Fe, Zn, Pb, Cd, and Cl. Chloride content is due to the impurities of the scrap (paints, rubbers and other by-products that are existing in packaging). A part of these impurities is transferred to the EAFD forming alkali metal chlorides (volatile organic compounds, VOCs) [24]. In most cases, the zinc content is present around 4–35 wt %, while iron varies from 25 to 50 wt % [25]. In the present case, the elemental analyses show that the compositions of both samples are very similar being Fe and Zn the more significant elements. However, even though Fe and Zn are mostly present in the sample's composition, in the case of the S-EAFD sample around 17 wt % of Cr was found, as expected according to the dust source.

XRD patterns of C-EAFD and S-EAFD dusts are shown in Fig. 1. In both samples, the majority of the diffraction maxima, marked in Fig. 1 with an asterisk, can be attributed to $ZnFe_2O_4$ with the cubic spinel structure (with space group Fd-3 m). Moreover, the peaks marked with a triangle can be indexed to ZnO with the hexagonal wurtzite structure (space group P63 mc). Low-intensity diffraction maxima were also detected.

Table 2 – Quantitative analyses from Rietveld analyses.

Crystallite phases (%)	C-EAFD	S-EAFD
$ZnFe_2O_4$ (zinc ferrite)	75	66
ZnO (zincite)	20	7
Others impurities (KCl; PbCl(OH))	5	----
$FeCr_2O_4$ (chromite)	----	27

In order to carry out a better structural characterization, Rietveld refinements of both samples were performed. Quantitative analyses are also shown in Table 2.

As can be seen, the obtained results show that the $ZnFe_2O_4$ and ZnO are present in both cases as majority phases. In the case of C-EAFD sample, the corresponding analysis exhibits approximately 5 % impurities as chlorides in different forms (KCl (sylvite) and PbCl(OH) (laurionite)). The result is in good agreement with the obtained from XRF analyses where the amount of Cl is higher in the C-EAFD sample. On the other hand, for the S-EAFD sample around 27 % of chromite was found. This result agrees again with the one obtained from XRF, where an amount of chromium was found in the corresponding analysis.

The intensity of the diffraction maxima is higher in the C-EAFD sample as compared with the S-EAFD sample showing a higher crystallinity. In addition, the average crystallite size

Table 3 – Raman bands positions observed and proposed assignments.

Peak position (cm^{-1}) [24,25]	C-EAFD	S-EAFD	Assignment
160	—	—	$F_{2g}(1)$
250	—	—	E_g
355	323	332	$T_{2g}(2)$
450	489	490	$T_{2g}(3)$
650	635	640	A_{1g}

(D_{hkl}) of both specks of dusts was calculated from Scherrer [26] equation (Eq. 1) using the most intense reflections observed in the XRD patterns:

$$D_{hkl} = \frac{0.89 \cdot \lambda}{\beta \cdot \cos\Theta} \quad (1)$$

where 0.89 is the shape factor (assuming spherical particles), λ is the X-ray wavelength, β is the full-width at half-maximum (FWHM) of the experimental peaks, θ is the Braggś angle.

The average crystallite sizes of both samples are within a range from 70 nm (C-EAFD) to 50 nm (S-EAFD). Larger crystallite size is found in C-EAFD sample, which confirms the observed trend of larger particle size in the sample with a higher degree of crystallinity.

Fig. 2 shows scanning electron microscopy micrographs for C-EAFD and S-EAFD samples obtained. In both samples, the particle shape is very similar. Two different particle morphologies can be appreciated. Mainly, agglomerates of globular morphology particles can be observed. As previously reported [4,27], the observed morphology is characteristic of the electric arc furnace flue dusts. This shape suggested that the mechanism of particle formation could be the ejection from the liquid metal and slag [27]. Also, octahedral crystals, typical of spinel structure phases [28,29] were also found in both samples due to the presence of $ZnFe_2O_4$ phases [30]. Finally, regarding the size of the constituent particles, and despite the fact that the particle size distribution is broad, larger particles were observed in the C-EAFD sample images compared with the other dusts. This result is in agreement with the XRD results where the C-EAFD sample exhibit higher diffraction maxima, i.e., greater crystallinity and particle size.

Fig. 3 shows the normalized Raman spectra of C-EAFD and S-EAFD samples. Table 3 summarized the observed Raman bands. Their corresponding assignments are also shown.

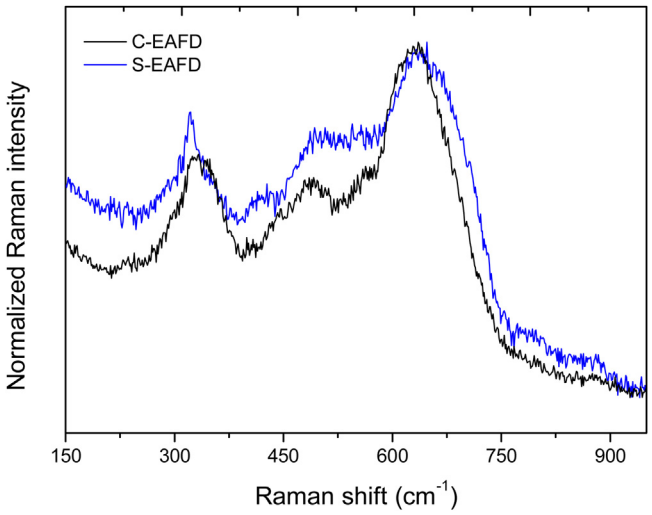

Fig. 3 – Normalized Raman spectra of the C-EAFD and S-EAFD samples.

In bulk, $ZnFe_2O_4$ is a normal spinel structure with cubic symmetry and Fd3 m (O^7_h) space group. Zn^{2+} divalent ions preferentially occupy the tetrahedral (A) sites, whereas, all the Fe^{3+} ions occupy octahedral (B) sites. Group theory predict five Raman-active modes ($A_{1g} + E_g + 3T_{2g}$) at RT [30,31]. These Raman-active modes are related to the motion of oxygen ions and both the A-site and B-site ions in the spinel structure.

High-frequency modes appear peaked at 650 cm^{-1}, 450 cm^{-1} and 355 cm^{-1} and can be attributed to A_{1g}, $T_{2g}(3)$ and $T_{2g}(2)$ modes, respectively [30,31]. Raman bands in the low energy region are due to the E_g mode at about 250 cm^{-1} and to the $F_{2g}(1)$ translational movement of the whole tetrahedron at 160 cm^{-1}. The A_{1g} mode represents the symmetric stretch of oxygen atoms along Fe-O tetrahedral bonds, whereas the E_g and $T_{2g}(3)$ modes are due to symmetric and asymmetric bending of oxygen with respect to Fe, respectively. The $T_{2g}(2)$ represents the asymmetric stretch of Fe-O bond and $T_{2g}(1)$ represents the translational movement of the tetrahedron (Fe_3O_4) [30,31]. However as observed in the spectra from Fig. 3 and in the data presented in Table 3, the position of the Raman peaks is shifted with respect to those observed in bulk material. $ZnFe_2O_4$ spinel ferrite with a nanoparticle size, the distribution of Zn^{2+} ions and Fe^{3+}

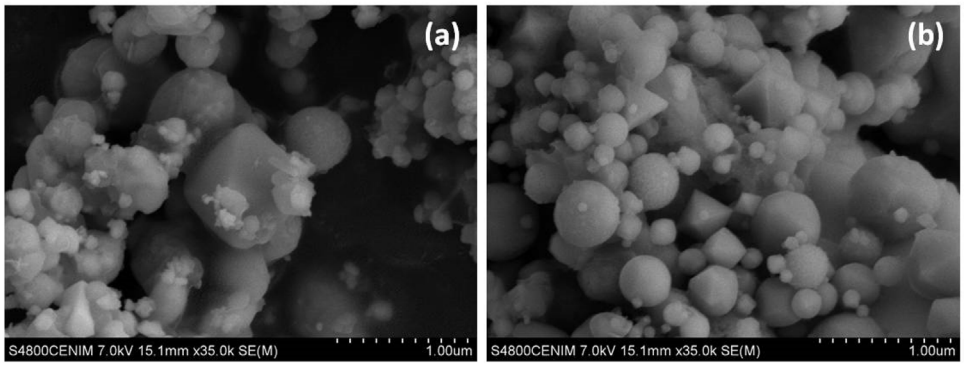

Fig. 2 – SEM images of the (a) C-EAFD and (b) S-EAFD investigated dust samples.

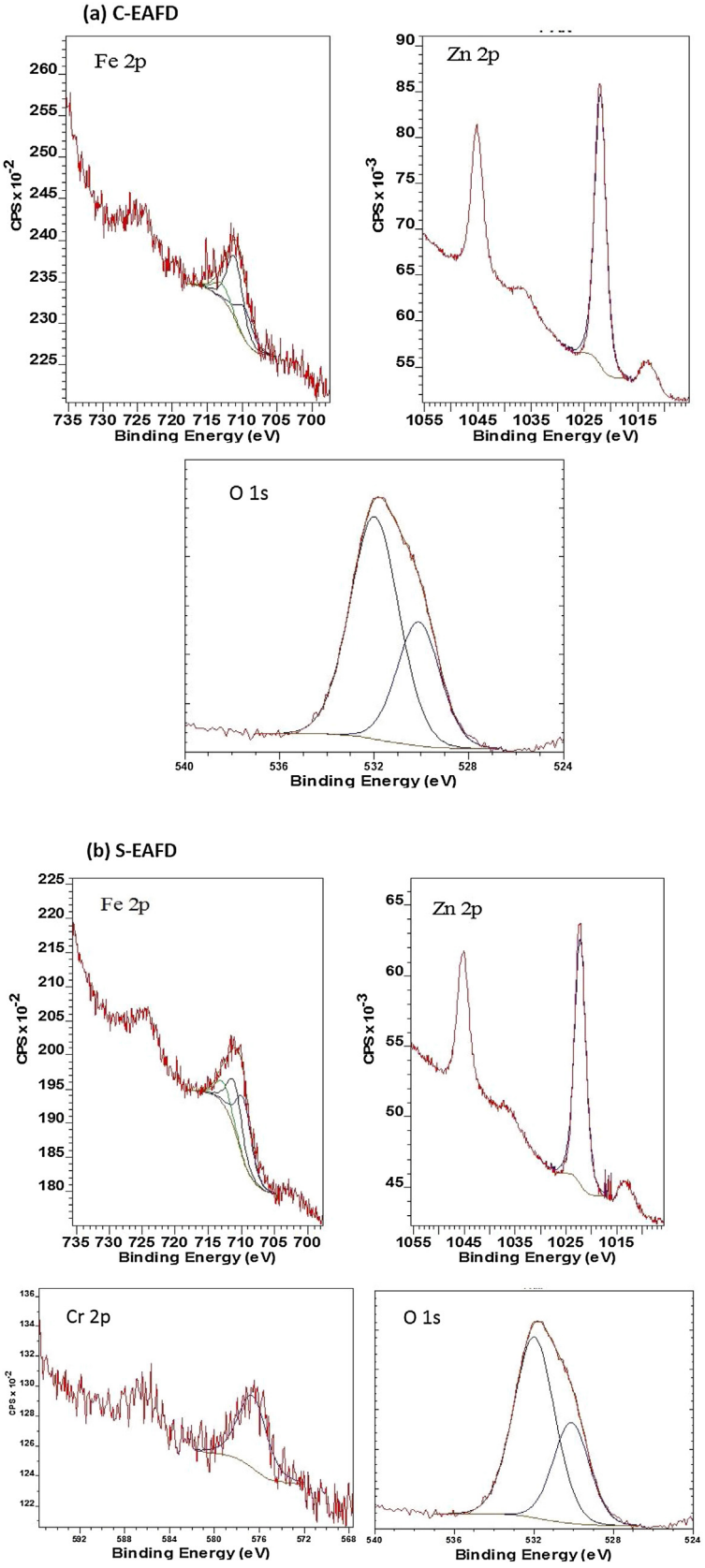

Fig. 4 – XPS spectra of Zn 2p, Fe 2p; O 1s and Cr 2p for (a) C-EAFD and (b) S-EAFD samples.

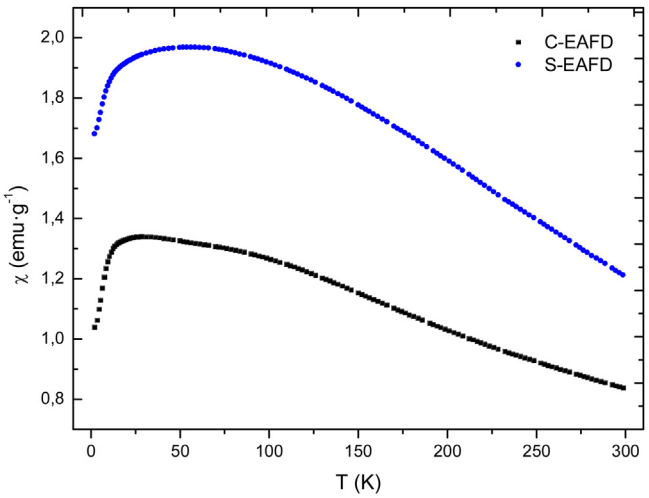

Fig. 5 – M vs T for the samples investigated.

cations among the tetrahedral (A) and octahedral (B) sites is altered, leading to a partially inverted spinel structure, $(Zn^{2+}_{1-x}Zn^{3+}_{x})[Zn^{2+}_{x}Zn^{3+}_{1-x}]O_4$ (where 'x' is inversion parameter) [30]. It is known that the *x* parameter is directly related to surface effect due to the reduction of grain size, and also with synthesis parameters and methods. So, in the present case, the observed shift in the Raman bands maxima could be since the spinel phases present a certain inversion degree.

On the other hand, a broadening of the Raman bands can be appreciated in the S-EAFD sample which is consistent with the lower crystallinity and smaller crystallite size of this dusts observed by XRD and SEM images, respectively.

The XPS spectra of Fe 2p and Zn 2p of the C-EAFD and S-EAFD samples are displayed in Fig. 4. In the case of the Fe, two intense peaks can be observed centered at around 711 eV and 725 eV that could be assigned to Fe $2p^{3/2}$ and Fe $2p^{1/2}$, of Fe^{3+}, respectively [32]. Also, in both cases, the peak at 711 eV can be deconvoluted in three component (at 709.6 eV, 711.0 eV, and 712.8 eV), and can be attributed to FeO or divalent Fe, Fe_2O_3 or trivalent Fe and a FeOOH, respectively [33]. In the case of XPS analysis of Zn 2p, two prominent peaks at 1021.5 eV and 1045.0 eV were also observed which corresponds to $2p^{3/2}$ and $2p^{1/2}$ [34]. XPS analyses of the Fe and Zn show that the peak of $2p^{3/2}$ is more intense than that of $2p^{1/2}$. This behavior is due to that the transitional metallic elements, the $2p^{3/2}$ state has four degeneracy states, while $2p^{1/2}$ state only has two [32]. In addition, for the S-EAFD sample, the 2p Cr XPS spectrum reveals only chromium in the 3+ oxidation state [35]. Finally, the O 1s spectrum exhibits two components at around 532 eV and 530 eV. The major peak (centered at 532 eV) was assigned to absorbed water molecules (O—H) [36], while the peak at 530 eV was in good agreement with the oxygen bonded to metal ion in $ZnFe_2O_4$ [34,37].

Magnetic susceptibility (χ) as a function of temperature (T) for both, C-EAFD and S-EAFD investigated samples, is shown in Fig. 5. A maximum centered on 25̃ K and 50̃ K for C-EAFD and S-EAFD, respectively, can be appreciated. This maximum temperature can be identified as the blocking temperature (T_B), and it is characteristic for either superparamagnetic (SP) or spin glass (SG) states [38,39]. Ferrimagnetic behavior below a T_B was observed.

Magnetic field dependence of magnetization (M vs. H) at RT for both samples is displayed in Fig. 6. As can be appreciated (Fig. 6 inset), the samples exhibit practically no hysteresis at 300 K, with a coercive field of 45 Oe.

3.2. *Cathodoluminescence (CL)*

In $ZnFe_2O_4$ phases, iron ions are usually incorporated into the ZnO matrix as Fe^{2+} and Fe^{3+}. Fe^{2+} ion has d^6 electronic configuration with the free ion ground state ^5D. In the case of the Fe^{3+}, the free ion has d^5 electronic configuration [40]. The ground state is ^6S, and the first excited state is ^4G. Into the ZnO matrix, the levels associated to Fe^{2+} and Fe^{3+} free ions could

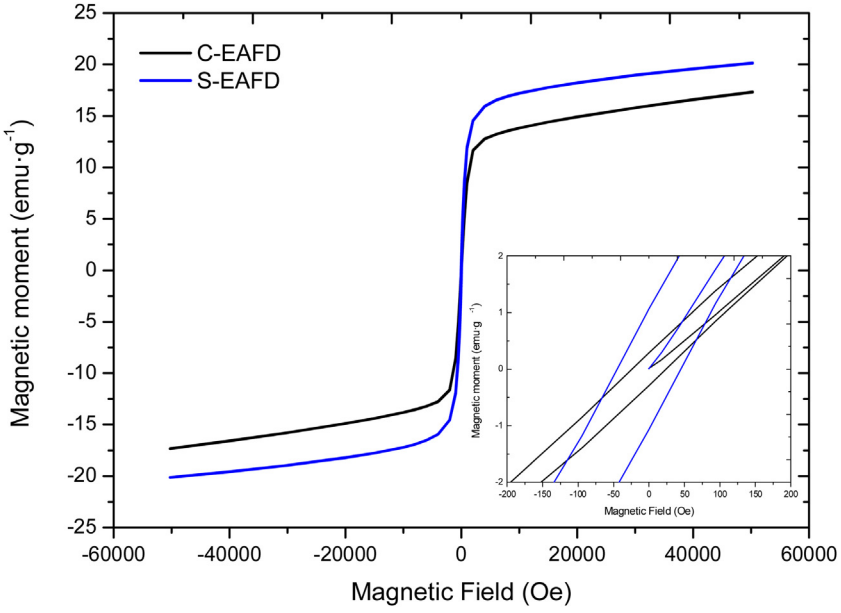

Fig. 6 – Magnetic hysteresis loops for C-EAFD and S-EAFD samples.

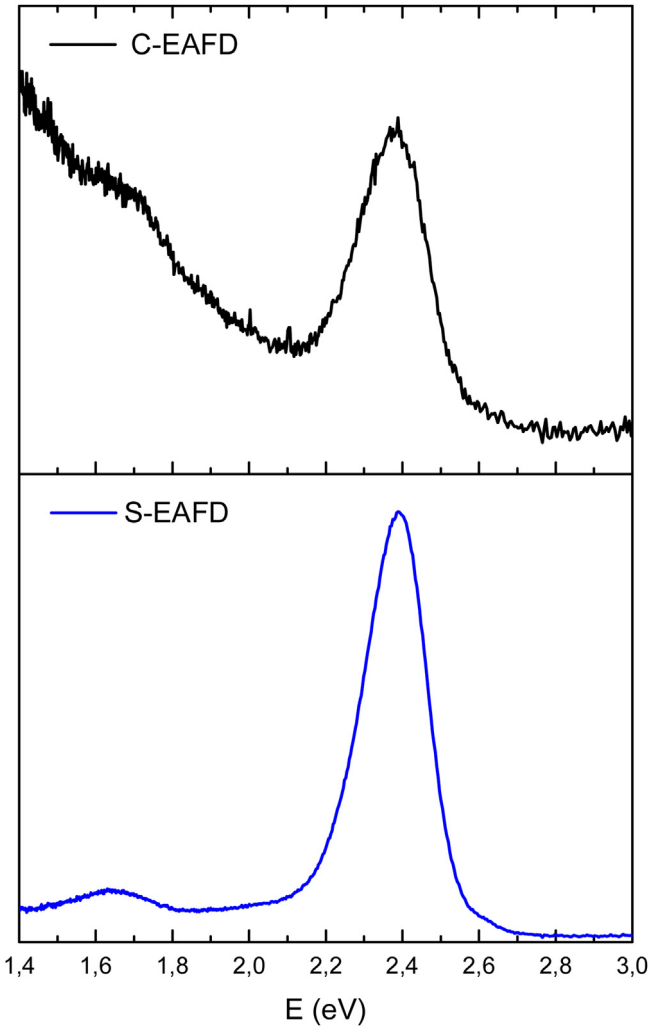

Fig. 7 – CL emission spectra of both waste dust samples.

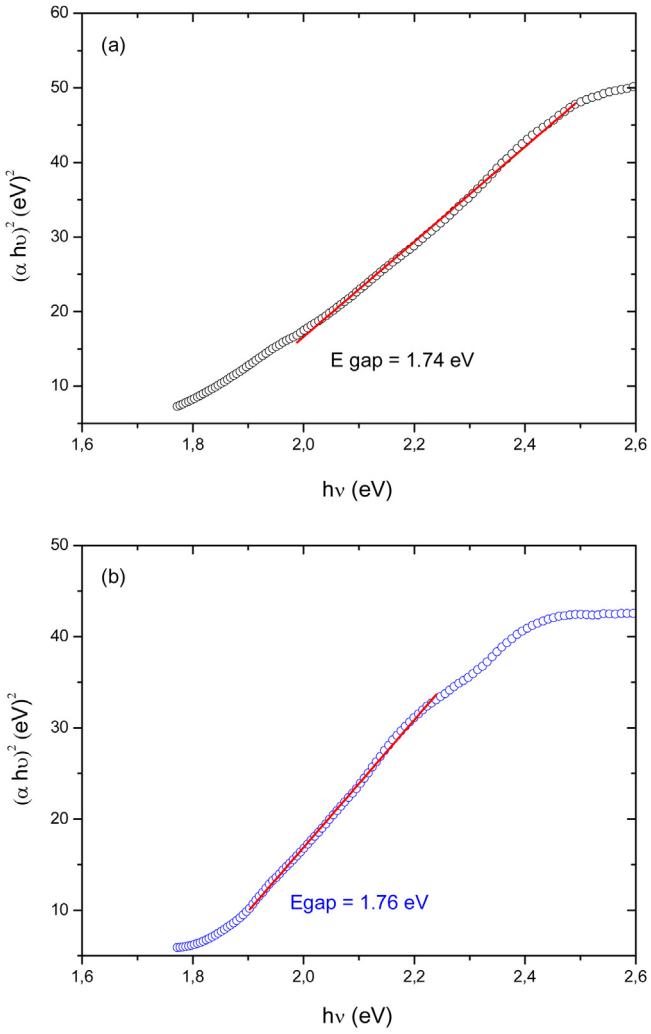

Fig. 8 – Kubelka-Munk function $(\alpha h\nu)^2$ versus photon energy ($h\nu$) for (a) C-EAFD and (b) S-EAFD samples.

be degenerated by crystal field perturbation, spin-orbit interaction and Jahn-Teller effect into the ^5E ground state term and the $^5T_2$ excited state term (for the Fe^{2+} ions) and transforms the ^6S ground state into a $^6A_1(S)$ state, where the first excited state is fourfold degenerated with the $^4T_1(G)$ term as the lowest state (to the Fe^{3+} ions) [40].

In addition, ZnO CL emission spectra are characterized by two typical features: the near-band-edge (NBE) emission at 3.25 eV, due to band-to-band transitions including bound excitons and shallow levels, and the intra-gap states related green luminescence (GL) band centered at 2.5 eV [41,42].

CL emission spectra of both samples at RT are shown in Fig. 7. A sharp band at 2.37 eV and a broad one at 1.71 eV are observed in both spectra. These bands could be related to a higher contribution of a spinel phase to luminescence emission [43] and to the phonon-assisted sideband of the intraionic transition $^4T_1(G)$-$^6A_1(S)$ of the Fe^{3+} ion [44], respectively. In the case of the Fe^{2+} emission, the transition from the ground state to the excited state term was observed in the far infrared region. Due to the fact that this region is outside of our luminescence sensitivity range, the optical properties of the Fe^{2+} ion emission could not be detected [40].

3.3. *Optical band gap measurements*

The optical band gap has been obtained from UV-Vis absorption experiments in DRS mode. In order to obtain the energy of the band gap for each of the samples, the Kubelka-Munk and Tauc approaches were used [45,46].

The Kubelka-Munk equation (Eq. 2) is first used to obtain absorption data from the diffuse reflectance spectrum:

$$F(R_\infty) = \frac{(1 - R_\infty)^2}{2R_\infty} \quad (2)$$

where R_∞ is the reflectance of an infinite film, and the function $F(R_\infty)$ is equivalent to the absorption coefficient, α.

So, the optical band gap (E_{gap}) can be calculated by extrapolation of the linear part of the curve $(\alpha h\nu)^2$ versus $h\nu$, as shown in Fig. 8.

The calculated band gap values were 1.74 eV and 1.76 eV for C-EAFD and S-EAFD samples, respectively. As compared with the optical band gap for bulk $ZnFe_2O_4$ (1.9 eV) the estimated values are slightly lower and very similar to those for $ZnFe_2O_4$ nanoparticles (≈1.77 eV) [47]. The decrease in the band gap

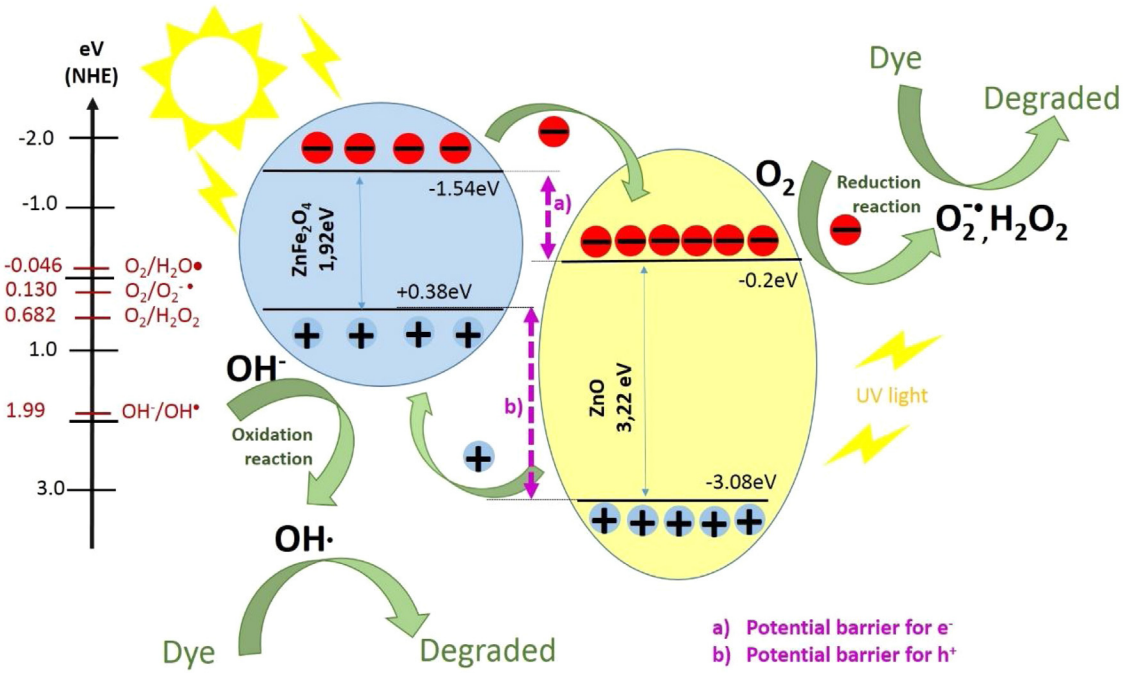

Fig. 9 – Schematic diagram of the photocatalytic process.

might be ascribed to additional sub-band-gap energy levels induced by the abundant surface and interface defects in the agglomerated nanoparticles [48]. In addition, these results could be beneficial to enhance photocatalytic activity [49].

3.4. *Photocatalytic activity*

The photocatalytic activity of C-EAFD and S-EAFD samples was investigated by MB degradation. When a photocatalyst absorbs light, a photocatalytic reaction takes place in several steps. The photocatalytic degradation process mechanisms are based on: i) formation of the charge carriers over the valence band (VB) and conduction band (CB) when the incident of light is at same or higher energy than the energy bandgap (E_g); ii) a possible recombination process of the e^-/h^+ pairs previously photogenerated, since these charge carriers are not stable, some of them some of them can recombinate producing heat in the process; iii) capture of photogenerated charge carriers transferred to the active sites on the surface of the photocatalyst producing redox reactions which leads to the formation of some active species (e.g. $\cdot O_2^-$, ·OH) capable of initiating following redox reactions and lastly; iv) the principal photocatalytic reactions which produce the degradation of pollutants, contaminants or organic molecules, breaking them down into innocuous and simple compounds [50,51]. Normally, as previously reported by others authors [52,53], these strong radicals decompose the dye to H_2O, CO_2 and mineral acids. Fig. 9 schematically describes the described process.

Fig. 10a and Fig. 10b show comparative MB spectra without light (a) and only light irradiation without photocatalysts (b) for 0 min and 120 min of exposure time. As can be appreciated, the intensity of the MB maxima bands does not decrease, indicating that the MB degradation does not occurs without the solid photocatalyst.

Fig. 10(c,d) exhibits the degradation curves of MB for both samples under UV irradiation for 120 min. In theses cases, two maxima centered at around 610 and 660 nm, characteristic of the MB absorption spectra, were registered [54]. As the UV irradiation exposure time increases, the intensity of the absorption maxima is decreased.

The kinetic of the degradation was adjusted to a pseudo-zero (Eq. 3), pseudo-first-order (Eq. 4) and pseudo-second-order (Eq. 5) [55] and the obtained results are summarized in Table 4.

$$\text{pseudo-zero-order } [C]_t = [C]_0 - k_{obs,0} \cdot t \tag{3}$$

$$\text{pseudo-first-order } \ln \frac{[C]_t}{[C]_0} = k_{obs,1} \cdot t \tag{4}$$

$$\text{pseudo-second-order } \frac{1}{[C]_t} = \frac{1}{[C]_0} + k_{obs,2} \cdot t \tag{5}$$

where $[C]_0$ is initial MB concentration; $[C]_t$ is the MB concentration at different time t and k_0, k_1 and k_2 are the kinetics constants to the pseudo-zero, pseudo-first and pseudo-second-order, respectively.

The correlation coefficients R^2 show that reaction kinetics fit better to the pseudo-first-order model.

The degradation percentage rates are shown in Fig. 11. The maximum degradation is obtained after 120 min of UV irradiation, time that the percentage remains practically constant. Also, the maximum degradation of the obtained samples was 80 % and 75 % for C-EAFD and S-EAFD samples, respectively. It is known that ZnO is an excellent photocatalytic material [56,57]. XRD results found that C-EAFD sample exhibits a more considerable ZnO amount compared with S-EAFD sample.

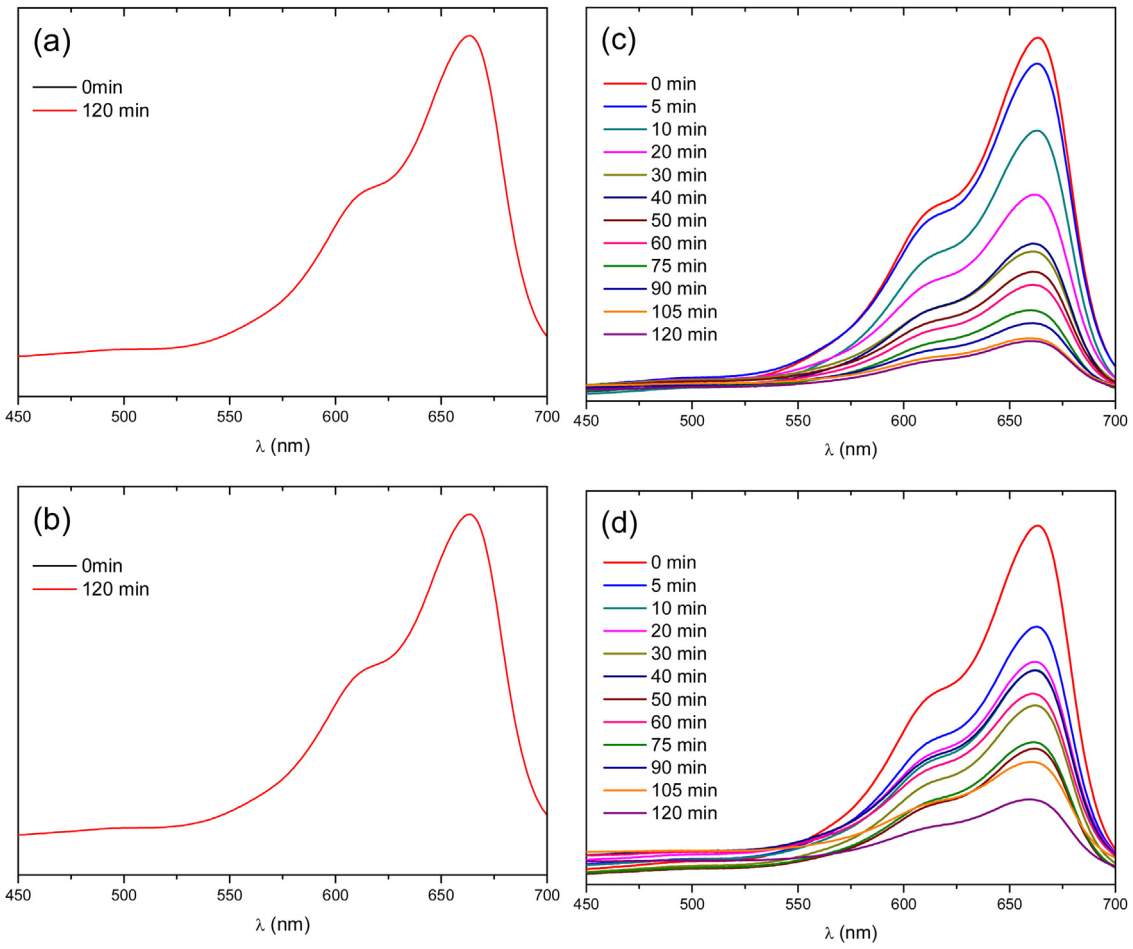

Fig. 10 – UV-Vis absorption spectra as a function of the reaction time for (a) MB without light; (b) only UV irradiation without photocatalysts; (c) UV irradiation with C-EAFD sample and (d) UV irradiation with S-EAFD sample.

Table 4 – Kinetics constants and R-factors calculated for both samples with MB solutions.

	Pseudo-zero order		Pseudo-first order		Pseudo-second order	
	k_0	R^2	k_1	R^2	k_2	R^2
C-EAFD	0,003	0,879	0,015	0,984	0,107	0,971
S-EAFD	0,019	0,894	0,011	0,957	0,080	0,884

So, the obtained degradation percentages agreed with these results.

Photocatalytic activity of the electric-arc furnace flue dusts have scarcely been assessed, previous investigations have been performanced in order to degrade different dyes using these type of samples as photocatalyst. In this sense, Sapiña et al. [58] have been evaluated the potential of EAFD as photocatalytic material in the degradation of rhodamine B (RhB) in the aqueous solution under UV/visible light irradiation. Similarly, the use of activated electric arc furnace slag for the photodegradation of methylene blue (MB) and acid blue 29 (AB29) was studied by Nasuha et al. [59]. These results previously reported exhibit that these type of the materials from steel production wastes could successfully be used as photocatalyst.

4. Conclusions

Two different electric-arc furnace flue dusts (EAFD), one of them from common steel manufacturing and another one from the manufacturing of special steel (C-EAFD and S-EAFD, respectively) have been characterized by several techniques. XRF analysis show that Fe and Zn are in major concentration in the composition of the samples. Structural characterization by Rietveld refinements reveals that $ZnFe_2O_4$ and ZnO phases are present in both cases as majority phases. Particles agglomerates with a globular and octahedral shape were found in SEM micrographs, in good agreement with the origin of the samples. Raman spectra showed several bands which can be attributed to spinel structure. In addition, CL emission due to

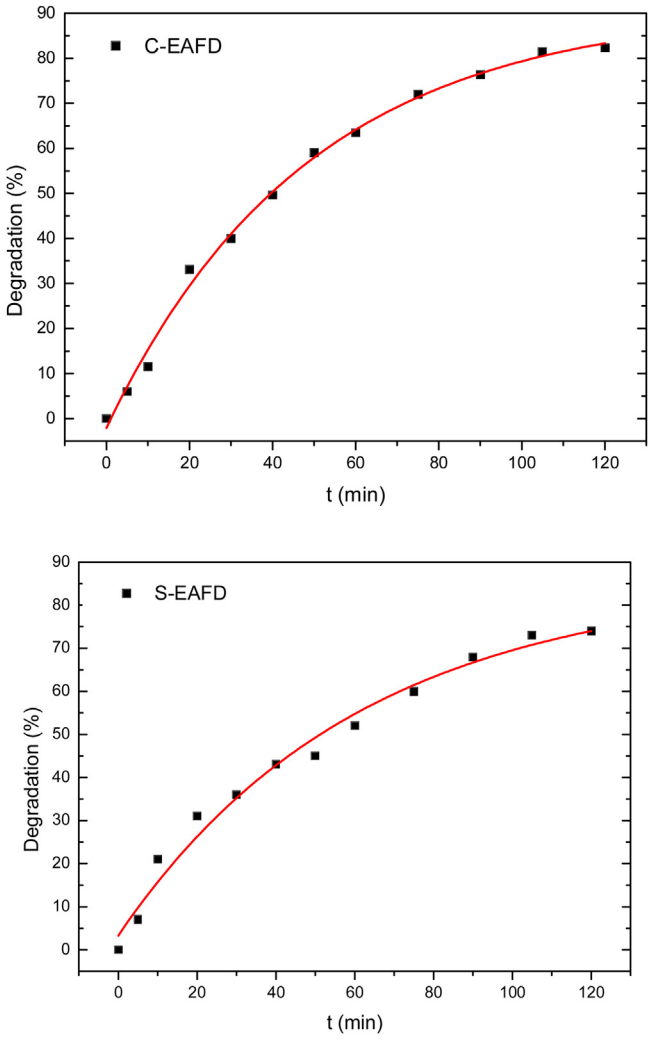

Fig. 11 – Degradation percentages for both samples investigated under UV irradiation to MB solutions.

spinel phase was also detected, as well as Fe^{3+} emission into ZnO structure characteristic of the $ZnFe_2O_4$ stoichiometry. T_B values around 25 K for C-EAFD sample and 50 K for S-EAFD sample were found in the magnetic measurements. Moreover, practically no coercive field has been detected from the hysteresis loops registered for the investigated samples. The calculated band gap values from Kubelka-Munk and Tauc's approaches were 1.74 eV and 1.76 eV for the C-EAFD and S-EAFD samples, respectively. These results are in good agreement with the corresponding to the $ZnFe_2O_4$ phase. Finally, the photocatalytic activity was also assessed. A decrease of the UV-Vis absorption maximum spectra of MB was found with the irradiation time increase, which indicates that MB degradation occurs. Kinetic study reveals that the reactions were better a fitted to the pseudo-second-order model. In addition, a degradation degree at around 75 % and 80 % for 120 min was found for C-EAFD and S-EAFD samples, respectively.

Conflicts of interest

The authors declare no conflicts of interest

Acknowledgment

This work has been partially supported by Spanish Ministry of Economy (MINECO) and Business and European Regional Development Fund (FEDER) (Grant ID MAT 2015-65274-R) and by the Comunidad de Madrid Program MULTIMAT CHALLENGE (Grant ID S2013/MIT-2862).

REFERENCES

[1] López F, Gonzalez P, Sainz E, Balcazar N. Electric arc furnace flue dust. Characterization and toxicity with Photobacterium phosphoreum. Int J Environ Pollut 1993;3:269–83, http://dx.doi.org/10.1504/IJEP.1993.028521.
[2] de Buzin PJWK, Heck NC, Vilela ACF. EAF dust: an overview on the influences of physical, chemical and mineral features in its recycling and waste incorporation routes. J Mater Res Technol 2017;6:194–202, http://dx.doi.org/10.1016/j.jmrt.2016.10.002.
[3] Nyirenda RL. The processing of steelmaking flue-dust: a review. Miner Eng 1991;4:1003–25, http://dx.doi.org/10.1016/0892-6875(91)90080-F.
[4] Machado JGMS, Brehm FA, Moraes CAM, dos Santos CA, Vilela ACF, et al. Chemical, physical, structural and morphological characterization of the electric arc furnace dust. J Hazard Mater 2006;136:953–60, http://dx.doi.org/10.1016/j.jhazmat.2006.01.044.
[5] de Araújo JA, Schalch V. Recycling of electric arc furnace (EAF) dust for use in steel making process. J Mater Res Technol 2014;3:274–9, http://dx.doi.org/10.1016/j.jmrt.2014.06.003.
[6] Chang MB, Huang CK. Characteristics of chlorine and carbon flow in two municipal waste incinerators in Taiwan. J Environ Eng (New York) 2002;128:1182–7, http://dx.doi.org/10.1061/(ASCE)0733-9372(2002)128:12(1182).
[7] López FA, López-Delgado A. Enhancement of electric arc furnace dust by recycling to electric arc furnace. J Environ Eng (New York) 2002;128:1169–74, http://dx.doi.org/10.1061/(ASCE)0733-9372(2002)128:12(1169).
[8] Rösler G, Pichler C, Antrekowitsch J, Wegscheider S. "2sDR": process development of a sustainable way to recycle steel mill dusts in the 21st century. Jom 2014;66:1721–9, http://dx.doi.org/10.1007/s11837-014-1131-8.
[9] Ibrahim M, El-Naas M, Benamor A, Al-Sobhi S, Zhang Z. Carbon mineralization by reaction with steel-making waste: a review. Processes 2019;7:115, http://dx.doi.org/10.3390/pr7020115.
[10] Sun L, Li J, Wang C, Li S, Lai Y, Chen H, et al. Ultrasound aided photochemical synthesis of Ag loaded TiO_2 nanotube arrays to enhance photocatalytic activity. J Hazard Mater 2009;171:1045–50, http://dx.doi.org/10.1016/j.jhazmat.2009.06.115.
[11] Hasija V, Sudhaik A, Raizada P, Hosseini-Bandegharaei A, Singh P. Carbon quantum dots supported AgI /ZnO/phosphorus doped graphitic carbon nitride as Z-scheme photocatalyst for efficient photodegradation of 2, 4-dinitrophenol. J Environ Chem Eng 2019;7:103272, http://dx.doi.org/10.1016/j.jece.2019.103272.
[12] Raizada P, Priya B, Thakur P, Singh P. Solar light induced photodegradation of oxytetracyline using Zr doped

TiOTiO$_2$/CaO based nanocomposite. Indian J Chem - Sect A Inorganic, Phys Theor Anal Chem 2016;55A: 803–9.
[13] Shandilya P, Mittal D, Soni M, Raizada P, Lim JH, Jeong DY, et al. Islanding of EuVO$_4$ on high-dispersed fluorine doped few layered graphene sheets for efficient photocatalytic mineralization of phenolic compounds and bacterial disinfection. J Taiwan Inst Chem Eng 2018;93:528–42, http://dx.doi.org/10.1016/j.jtice.2018.08.034.
[14] Li X, Hou Y, Zhao Q, Teng W, Hu X, Chen G. Capability of novel ZnFe$_2$O$_4$ nanotube arrays for visible-light induced degradation of 4-chlorophenol. Chemosphere 2011;82:581–6, http://dx.doi.org/10.1016/j.chemosphere.2010.09.068.
[15] Laokul P, Amornkitbamrung V, Seraphin S, Maensiri S. Characterization and magnetic properties of nanocrystalline CuFe$_2$O$_4$, NiFe$_2$O$_4$, ZnFe$_2$O$_4$ powders prepared by the Aloe vera extract solution. Curr Appl Phys 2011;11:101–8, http://dx.doi.org/10.1016/j.cap.2010.06.027.
[16] Su J, Shang Q, Guo T, Yang S, Wang X, Ma Q, et al. Construction of heterojunction ZnFe$_2$O$_4$/ZnO/Ag by using ZnO and Ag nanoparticles to modify ZnFe$_2$O$_4$ and its photocatalytic properties under visible light. Mater Chem Phys 2018;219:22–9, http://dx.doi.org/10.1016/j.matchemphys.2018.08.003.
[17] Gautam S, Shandilya P, Singh VP, Raizada P, Singh P. Solar photocatalytic mineralization of antibiotics using magnetically separable NiFe$_2$O$_4$ supported onto graphene sand composite and bentonite. J Water Process Eng 2016;14:86–100, http://dx.doi.org/10.1016/j.jwpe.2016.10.008.
[18] Singh P, Gautam S, Shandilya P, Priya BP, Singh V, Raizada P. Graphene bentonite supported ZnFe$_2$O$_4$ as superparamagnetic photocatalyst for antibiotic degradation. Adv Mater Lett 2017;8:229–38, http://dx.doi.org/10.5185/amlett.2017.1467.
[19] Raizada P, Singh P, Kumar A, Sharma G, Pare B, Jonnalagadda SB, et al. Solar photocatalytic activity of nano-ZnO supported on activatedcarbon or brick grain particles: role of adsorption in dye degradation. Appl Catal A Gen 2014;486:159–69, http://dx.doi.org/10.1016/j.apcata.2014.08.043.
[20] Raizada P, Sudhaik A, Singh P. Photocatalytic water decontamination using graphene and ZnO coupled photocatalysts: a review. Mater Sci Energy Technol 2019;2:509–25, http://dx.doi.org/10.1016/j.mset.2019.04.007.
[21] Dutta V, Singh P, Shandilya P, Sharma S, Raizada P, Saini AK, et al. Review on advances in photocatalytic water disinfection utilizing graphene and graphene derivatives-based nanocomposites. J Environ Chem Eng 2019;7:103132, http://dx.doi.org/10.1016/j.jece.2019.103132.
[22] Shi W, Guo F, Wang H, Liu C, Fu Y, Yuan S, et al. Carbon dots decorated magnetic ZnFe2O4nanoparticles with enhanced adsorption capacity for the removal of dye from aqueous solution. Appl Surf Sci 2018;433:790–7, http://dx.doi.org/10.1016/j.apsusc.2017.10.099.
[23] Sofilić T, Rastovčan-Mioč A, Cerjan-Stefanović Š, Novosel-Radović V, Jenko M. Characterization of steel mill electric-arc furnace dust. J Hazard Mater 2004;109:59–70, http://dx.doi.org/10.1016/j.jhazmat.2004.02.032.
[24] Raupenstrauch H, Doschek-Held K, Rieger J, Reiter W. RecoDust—an efficient way of processing steel mill dusts. J Sustain Metall 2019, http://dx.doi.org/10.1007/s40831-019-00216-y.
[25] Suetens T, Guo M, Van Acker K, Blanpain B. Formation of the ZnFe$_2$O$_4$ phase in an electric arc furnace off-gas treatment system. J Hazard Mater 2015;287:180–7, http://dx.doi.org/10.1016/j.jhazmat.2015.01.050.
[26] Patterson AL. The scherrer formula for X-Ray particle size determination. Phys Rev 1939;56:978–82, http://dx.doi.org/10.1103/PhysRev.56.978.
[27] da Silva MC, Bernardes AM, Bergmann CP, Tenório JAS, Espinosa DCR. Characterisation of electric arc furnace dust generated during plain carbon steel production. Ironmak Steelmak 2008;35:315–20, http://dx.doi.org/10.1179/030192307X232936.
[28] Yadav NG, Chaudhary LS, Sakhare PA, Dongale TD, Patil PS, Sheikh AD. Impact of collected sunlight on ZnFe$_2$O$_4$ nanoparticles for photocatalytic application. J Colloid Interface Sci 2018;527:289–97, http://dx.doi.org/10.1016/j.jcis.2018.05.051.
[29] Romo LA, López-Fernández A, García-Díaz I, Fernández P, Urbieta A, López FA. From spent alkaline batteries to Zn$_x$Mn$_{3-x}$O$_4$ by a hydrometallurgical route: synthesis and characterization. RSC Adv 2018;8:33496–505, http://dx.doi.org/10.1039/C8RA06789A.
[30] Yadav RS, Kuřitka I, Vilcakova J, Urbánek P, Machovsky M, Masař M, et al. Structural, magnetic, optical, dielectric, electrical and modulus spectroscopic characteristics of ZnFe$_2$O$_4$ spinel ferrite nanoparticles synthesized via honey-mediated sol-gel combustion method. J Phys Chem Solids 2017;110:87–99, http://dx.doi.org/10.1016/j.jpcs.2017.05.029.
[31] Bini M, Tondo C, Capsoni D, Mozzati MC, Albini B, Galinetto P. Superparamagnetic ZnFe$_2$O$_4$ nanoparticles: the effect of Ca and Gd doping. Mater Chem Phys 2018;204:72–82, http://dx.doi.org/10.1016/j.matchemphys.2017.10.033.
[32] Chen M, Liu D, Deng Y, Fu W, Zou H, Liang F. Tailoring the porosity of ZnO/ZnFe$_2$O$_4$ composites for photocatalytic applications. Ceram Int 2017;43:16027–31, http://dx.doi.org/10.1016/j.ceramint.2017.08.148.
[33] Yamashita T, Hayes P. Analysis of XPS spectra of Fe^{2+} and Fe^{3+} ions in oxide materials. Appl Surf Sci 2008;254:2441–9, http://dx.doi.org/10.1016/j.apsusc.2007.09.063.
[34] Ameer S, Gul IH, Mahmood N, Mujahid M. Synthesis, characterization and optical properties of in situ ZnFe$_2$O$_4$ functionalized rGO nano hybrids through modified solvothermal approach. Opt Mater (Amst) 2015;45:69–75, http://dx.doi.org/10.1016/j.optmat.2015.02.035.
[35] Biesinger MC, Brown C, Mycroft JR, Davidson RD, McIntyre NS. X-ray photoelectron spectroscopy studies of chromium compounds. Surf Interface Anal 2004;36:1550–63, http://dx.doi.org/10.1002/sia.1983.
[36] Chiang CL, Lin KS, Hsu PJ, Lin YG. Synthesis and characterization of magnetic zinc and manganese ferrite catalysts for decomposition of carbon dioxide into methane. Int J Hydrogen Energy 2017;42:22123–37, http://dx.doi.org/10.1016/j.ijhydene.2017.06.033.
[37] Wang M, Sun L, Cai J, Huang P, Su Y, Lin C. A facile hydrothermal deposition of ZnFe$_2$O$_4$ nanoparticles on TiO$_2$ nanotube arrays for enhanced visible light photocatalytic activity. J Mater Chem A Mater Energy Sustain 2013;1:12082–7, http://dx.doi.org/10.1039/c3ta12577g.
[38] Zamiri R, Salehizadeh SA, Ahangar HA, Shabani M, Rebelo A, Suresh Kumar J, et al. Optical and magnetic properties of ZnO/ZnFe$_2$O$_4$ nanocomposite. Mater Chem Phys 2017;192:330–8, http://dx.doi.org/10.1016/j.matchemphys.2017.01.066.
[39] Martínez B, Roig A, Obradors X, Molins E, Rouanet A, Monty C. Magnetic properties of γ-Fe$_2$O$_3$ nanoparticles obtained by vaporization condensation in a solar furnace. J Appl Phys 1996;79:2580–6, http://dx.doi.org/10.1063/1.361125.
[40] Malguth E, Hoffmann A, Phillips MR. Fe in III-V and II-VI semiconductors. Phys Status Solidi Basic Res 2008;245:455–80, http://dx.doi.org/10.1002/pssb.200743315.
[41] Fabbri F, Villani M, Catellani A, Calzolari A, Cicero G, Calestani D, et al. Zn vacancy induced green luminescence on non-polar surfaces in ZnO nanostructures. Sci Rep 2014;4:1–6, http://dx.doi.org/10.1038/srep05158.

[42] Lazzarini L, Salviati G, Fabbri F, Zha M, Calestani D, Zappettini A, et al. Unpredicted nucleation of extended zinc blende phases in wurtzite ZnO nanotetrapod arms. ACS Nano 2009;3:3158–64, http://dx.doi.org/10.1021/nn900558q.
[43] Urbieta A, Fernández P, Piqueras J. Nanowires and stacks of nanoplates of Mn doped ZnO synthesized by thermal evaporation-deposition. Mater Chem Phys 2012;132:1119–24, http://dx.doi.org/10.1016/j.matchemphys.2011.12.084.
[44] Müller S, Zhou M, Li Q, Ronning C. Intra-shell luminescence of transition-metal-implanted zinc oxide nanowires. Nanotechnology 2009;20:135704, http://dx.doi.org/10.1088/0957-4484/20/13/135704.
[45] Nobbs JH. Kubelka-munk theory and the prediction of reflectance. Rev Prog Color Relat Top 2008;15:66–75, http://dx.doi.org/10.1111/j.1478-4408.1985.tb03737.x.
[46] Pal M, Pal U, Jiménez JMGY, Pérez-Rodríguez F. Effects of crystallization and dopant concentration on the emission behavior of TiO_2:Eu nanophosphors. Nanoscale Res Lett 2012;7:1, http://dx.doi.org/10.1186/1556-276X-7-1.
[47] Han L, Zhou X, Wan L, Deng Y, Zhan S. Synthesis of ZnFe2O_4 nanoplates by succinic acid-assisted hydrothermal route and their photocatalytic degradation of rhodamine B under visible light. J Environ Chem Eng 2014;2:123–30, http://dx.doi.org/10.1016/j.jece.2013.11.031.
[48] Kislov N, Srinivasan SS, Emirov Y, Stefanakos EK. Optical absorption red and blue shifts in $ZnFe_2O_4$ nanoparticles. Mater Sci Eng B 2008;153:70–7, http://dx.doi.org/10.1016/j.mseb.2008.10.032.
[49] Fu H, Zhang S, Xu T, Zhu Y, Chen J. Photocatalytic degradation of RhB by fluorinated Bi_2WO_6 and distributions of the intermediate products. Environ Sci Technol 2008;42:2085–91, http://dx.doi.org/10.1021/es702495w.
[50] Pirhashemi M, Habibi-Yangjeh A, Rahim Pouran S. Review on the criteria anticipated for the fabrication of highly efficient ZnO-based visible-light-driven photocatalysts. J Ind Eng Chem 2018;62:1–25, http://dx.doi.org/10.1016/j.jiec.2018.01.012.
[51] Kulkarni SD, Kumbar S, Menon SG, Choudhari KS, Santhosh C. Magnetically separable core-shell $ZnFe_2O_4$@ZnO nanoparticles for visible light photodegradation of methyl orange. Mater Res Bull 2016;77:70–7, http://dx.doi.org/10.1016/j.materresbull.2016.01.022.
[52] Güy N, Özacar M. Ag/Ag_2CrO_4 nanoparticles modified on ZnO nanorods as an efficient plasmonic photocatalyst under visible light. J Photochem Photobiol A: Chem 2019;370:1–11, http://dx.doi.org/10.1016/j.jphotochem.2018.10.035.
[53] Boutra B, Güy N, Özacar M, Trari M. Magnetically separable $MnFe_2O_4$/TA/ZnO nanocomposites for photocatalytic degradation of Congo Red under visible light. J Magn Magn Mater 2020;497:165994, http://dx.doi.org/10.1016/j.jmmm.2019.165994.
[54] Heger D, Jirkovský J, Klán P. Aggregation of methylene blue in frozen aqueous solutions studied by absorption spectroscopy. J Phys Chem A 2005;109:6702–9, http://dx.doi.org/10.1021/jp050439j.
[55] Gaya UI. Heterogeneous photocatalysis using inorganic semiconductor solids. Springer Netherlands: Dordrecht; 2014, http://dx.doi.org/10.1007/978-94-007-7775-0.
[56] Nagaraju G, Shivaraju GC, Banuprakash G, Rangappa D. Photocatalytic activity of ZnO nanoparticles: synthesis via solution combustion method. Mater Today Proc 2017;4:11700–5, http://dx.doi.org/10.1016/j.matpr.2017.09.085.
[57] Tian C, Zhang Q, Wu A, Jiang M, Liang Z, Jiang B, et al. Cost-effective large-scale synthesis of ZnO photocatalyst with excellent performance for dye photodegradation. Chem Commun (Camb) 2012;48:2858, http://dx.doi.org/10.1039/c2cc16434e.
[58] Sapiña M, Jimenez-Relinque E, Castellote M. Turning waste into valuable resource: potential of electric arc furnace dust as photocatalytic material. Environ Sci Pollut Res 2014;21:12091–8, http://dx.doi.org/10.1007/s11356-014-3167-2.
[59] Nasuha N, Ismail S, Hameed BH. Activated electric arc furnace slag as an effective and reusable Fenton-like catalyst for the photodegradation of methylene blue and acid blue 29. J Environ Manage 2017;196:323–9, http://dx.doi.org/10.1016/j.jenvman.2017.02.070.